




# Development and characterization of a new predominantly $\beta$ Ti–15Mo–5In alloy for biomedical applications

L. Romero-Resendiz<sup>1,2,\*</sup> , M. C. Rossi<sup>2,3</sup>, C. Seguí-Esquembre<sup>2</sup>, and V. Amigó-Borrás<sup>2</sup>

<sup>1</sup> Facultad de Química, Departamento de Ingeniería Metalúrgica, Universidad Nacional Autónoma de México, 04510 Mexico City, Mexico

<sup>2</sup> Universitat Politècnica de València, Instituto de Tecnología de Materiales, Camino de Vera s/n, 46022 Valencia, Spain

<sup>3</sup> Materials Engineering Department (DEMa), Universidade Federal de São Carlos (UFSCar), São Carlos, SP 13.565-905, Brazil

**Received:** 3 March 2023

**Accepted:** 3 October 2023

**Published online:**  
28 October 2023

© The Author(s), 2023

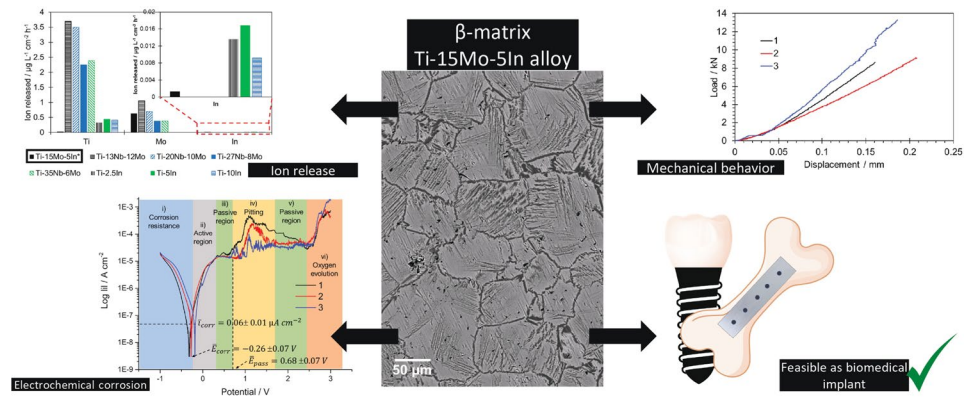
## ABSTRACT

A new Ti–Mo–In alloy was designed for biomedical implant applications and produced by powder metallurgy. Mechanical properties, ion release, and electrochemical assessments were conducted to uncover its biomaterial feasibility. The Ti–15Mo–5In alloy consisted of a nearly equiaxed and micrometric  $\beta$  matrix with acicular  $\alpha$  and fine dispersed  $\alpha''$  phases. Mo and In chosen contents encouraged flexural strength (0.59 GPa) and hardness (3.9 GPa) beyond the values for human bone in the literature. As expected from the predominantly  $\beta$  microstructure, a medium value of elastic modulus (80 GPa) was obtained. The ion Ti ( $0.019 \mu\text{gL}^{-1} \text{cm}^{-2} \text{h}^{-1}$ ), Mo ( $0.622 \mu\text{gL}^{-1} \text{cm}^{-2} \text{h}^{-1}$ ), and In ( $0.001 \mu\text{gL}^{-1} \text{cm}^{-2} \text{h}^{-1}$ ) released concentrations were below harmful concentrations to human health. Corrosion rates during immersion and electrochemical tests ( $0.524$  and  $0.1 \mu\text{m year}^{-1}$ , respectively) were lower than those reported for various implant materials. The Ti–15Mo–5In alloy is a feasible option for orthopedic and dental implants.

Handling Editor: Annela M. Seddon.

Address correspondence to E-mail: liliana.rom7@comunidad.unam.mx

## GRAPHICAL ABSTRACT



## Introduction

There is a high worldwide demand for dental and orthopaedic prosthetics. At least a 2.5-fold increment in the incidence rate of total knee arthroplasty, especially in male patients, is projected from 2020 to the 2050 year in Germany [1]. Even more disquieting projections are expected for primary total hip arthroplasties and total knee arthroplasties in the USA, with increments of 174% and 673%, respectively, from 2005 to 2030 [2]. The demand for dental implants is also high considering a prevalence increment from 5.7 to 23% projected for the 2026 year in the USA [3]. Consequently, the projection for periprosthetic joint infections and clinical revisions is expected to sharply increase in the following decades [1, 2]. Thus, the development of accessible, feasible, as well as mechanically and biologically improved implant materials, is a health and economic worldwide burden. Mechanical performance and biocompatibility (including ion release, corrosion, and low toxicity) are among the crucial factors for a material to be feasible for biomedical purposes.

Regarding the mechanical performance, the use of porous materials for biomedical implants is advantageous due to the lower elastic modulus compared to that of dense alloys. The mismatch of elastic modulus between the implant and the organic tissue promotes disuse osteoporosis or bone resorption due to stress shielding, i.e., the bone became unloaded [4, 5]. Due to the above, alloys with elastic modulus near to that of the human bone, 5–30 GPa [6, 7], increase

the efficiency of the implant. Besides, porosity assists in the fixation and ingrowth of organic tissue and improves the body fluid [6, 8]. Nevertheless, highly porous Ti alloys may have reduced corrosion resistance [9]. Therefore, porosity control is a key factor to select thermo-mechanical elaboration routes for implant materials. Press and sintering (P&S) technique allows functional porosity control [10–12], and it is the most competitive powder metallurgy method in terms of cost [13, 14].

Among the multiple porous metallic systems for biomedical purposes, Ti alloys are further the most reported and applied [15]. This is due to their biocompatibility, low toxicity, high mechanical resistance, and high corrosion resistance [12, 16]. Besides, they have lower elastic modulus than other metallic biomaterials such as Co–Cr or 316L stainless steel [4]. Besides, the Ni, Co, and Cr released from Co–Cr and 316L alloys are harmful to the human body [4]. Exploring different Ti-based alloy systems is a promising route for developing efficient and safe biomaterials.

One of the most employed Ti alloys for implants is the Ti–6Al–4V [11, 17]. However, V and Al have several harmful effects on human health [4, 18, 19]. To attend the previous shortcoming, different non-toxic porous Ti alloys have been developed, for example, Ti–Nb [20], Ti–Nb–Sn [21–23], Ti–In [24], Ti–Mo [25, 26], and Ti–Mo–Zr [26], among others. From the development of new biomaterials systems, Mo is advantageous for reducing the elastic modulus and increasing the corrosion resistance of Ti alloys without cytotoxic effects [27]. Moreover, the addition of In to porous Ti

alloys demonstrated non-toxic ion release concentrations and adequate mechanical performance without risky opposition to teeth [24]. From those results, the use of In and Mo as alloying elements on Ti alloys is emerging and they have been pointed out as promising candidates for orthopedic and dental implants. Despite its advantages, scarce information about the feasibility of porous Ti–Mo–In alloys for biomedical purposes has been reported.

This work aims to study the feasibility of a new porous Ti–15Mo–5In alloy for biomedical applications, specifically for dental and orthopedic implants. The chemical composition of the alloy was designed to promote a  $\beta$  phase matrix. The mechanical performance, ion release rate, and electrochemical behaviors were studied and correlated with the bi-phasic microstructure of the alloy. The development of the new Ti–15Mo–5In alloy may foster the exploration of different non-harmful, mechanically suitable, and biocompatible systems for biomedical implants.

## Materials and methods

### Preparation of the alloy by powder metallurgy technique

Elemental powders of Ti (29.2  $\mu\text{m}$ ), Mo (4.3  $\mu\text{m}$ ), and In (28.4  $\mu\text{m}$ ) purchased from Atlantic Equipment Engineers and Alpha Aesar were weighed according to the stoichiometric ratio in wt% of the Ti–15Mo–5In alloy. The Mo content was selected slightly up to the minimum to stabilize the  $\beta$ -Ti phase (~ 10 wt%) and enough In to ensure good mechanical and corrosion performances without segregation excess [24, 28]. Elemental powders were mixed in a 2-L Inversina BioEngineering mixer at 42  $\text{min}^{-1}$  for 45 min. Then, the powders were compacted uniaxially at 700 MPa to a geometry of 30  $\times$  12  $\times$  5 mm. Prior to sintering, the chamber of a Carbolite HVT 15-75-450 high vacuum tube furnace was filled with argon and evacuated twice. Sintering was performed at 0.03 Pa in two cycles: (a) heating at 10  $^{\circ}\text{C}/\text{min}$  and holding temperature at 780  $^{\circ}\text{C}$  for 60 min and (b) heating at 7  $^{\circ}\text{C}/\text{min}$  and holding temperature at 1300  $^{\circ}\text{C}$  for 180 min. Sintering finished by furnace cooling.

Prior to microstructural and electrochemical characterization, the samples were subjected to conventional metallographic preparation until mirror appearance

with a 90 vol% colloidal silica (0.04  $\mu\text{m}$  particle size) and 10 vol% hydrogen peroxide solution. The samples were cleaned with distilled water and ethyl alcohol for 15 min in an ultrasonic bath.

### Microstructural characterization

Phases identification and quantification was carried out in an Bruker/D2Phaser X-ray diffractometer with Cu  $K\alpha$  radiation at 30 kV and 10 mA. Step size of 0.02 $^{\circ}$  was used at a scanning speed of 0.0025 $^{\circ}$   $\text{s}^{-1}$ . Lattice parameters and quantitative estimation of phases were performed by Rietveld refinement in the MAUD software version 2.94. Porosity, phases distribution and morphology were studied by a Nikon Eclipse LV100DA optical microscope (OM) and a ZEISS-ULTRA 55 field emission scanning electron microscope (FESEM). An energy-dispersive X-ray spectroscopy (EDS) detector coupled to the FESEM was used for semi-quantitative elemental analyses. Crystallographic texture analyses were performed in an Oxford Instruments Ltda. electron backscatter diffraction detector (EBSD) coupled to the FESEM. Density and porosity were estimated according to the ASTM B328 standard by the three-dimensional Archimedes method.

### Mechanical behavior

At least, 5 microhardness measurements were obtained by applying 1.9 N for 10 s with a Shimadzu HMV tester. Three measurements of four-point flexural tests were performed in a Shimadzu Autograph AG-X plus 100 kN in samples with a geometry of 28  $\times$  11  $\times$  5 mm at a constant speed of 0.5  $\text{mm min}^{-1}$ . The distance between the lower and upper supports was 22 mm and 11 mm, respectively. A dynamic technique (ATCP) was used instead of mechanical methods to measure the elastic modulus with a higher precision [29]. Eight measurements of elastic modulus were obtained according to the ASTM-E1876 by the impulse excitation technique in an ATCP Sonelastic $^{\circledR}$ . The results were analyzed by the ATCP Sonelastic 3.0 software.

### Ion release and electrochemical evaluations

Three samples with an exposed area of 1.12  $\text{cm}^2$  were immersed in 50 mL of modified Ringer–Hartmann artificial saliva (5.97 NaCl, 0.37 KCl, 0.23  $\text{CaCl}_2$ , and 3.25

$C_3H_5O_3Na$  g L<sup>-1</sup>) with a pH of  $6.53 \pm 0.2$ . The immersion was performed at 37 °C for 730 h to imitate the oral environment during three 2-min daily brushings for 20 years [30]. The morphology of the tested samples was observed under OM and SEM. The inductively coupled plasma optical emission spectrometry (ICP-OES) technique was used by a Varian-715ES to measure the release concentrations of Ti, Mo, and In ions that remained in the test medium.

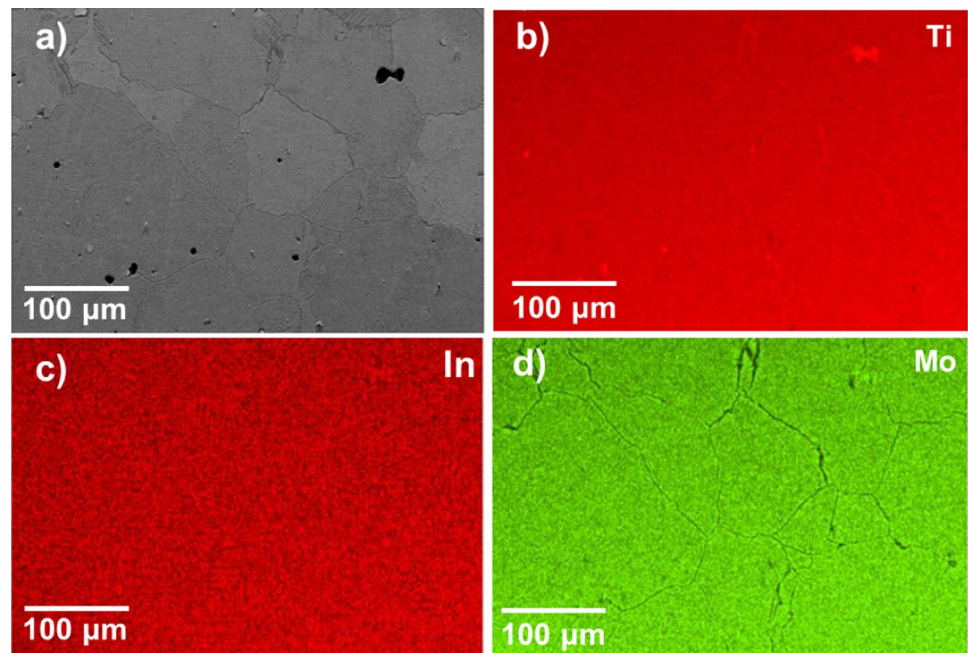
Electrochemical corrosion was studied by a potentiostat/galvanostat (Metrohm potentiostat-PGSTAT204) on three samples with a exposed surface of 0.785 cm<sup>2</sup>. An electrochemical cell with three electrodes was used with a modified Ringer-Hartmann solution electrolyte at 37 °C. Ag/AgCl, platinum, and Ti–15Mo–5In alloy were used as reference, auxiliary, and working electrodes, respectively. Open-circuit potential (OCP) measurements were performed for 1 h. Electrochemical impedance spectroscopy (EIS) analyses were performed at a wave amplitude of 0.01 V<sub>RMS</sub> and a frequency range of 100 kHz to 5 mHz. The results were registered by ZView software, and the electrochemical parameters calculations were done by the Tafel's extrapolation method in Wolfram Mathematica 12.1 software. A density of 5.03 g cm<sup>-3</sup> (method in Section "Microstructural characterization") was measured for the Ti–15Mo–5In alloy and was considered for electrochemical analyses.

## Results

### Microstructural characterization

The distribution of the constituent elements in the Ti–15Mo–5In alloy is shown in Fig. 1. The homogeneous microstructure suggested that the powders mixing, the selected sintering temperatures, and cooling rate were adequate to avoid solute segregation or heterogeneities through the material. There is scarce information on the ternary Ti–In–Mo system, but from the binary diagram phases of Ti–In and Ti–Mo [31, 32], a melting point  $\leq 1850$  °C can be expected for the Ti–15Mo–5In alloy. 70–90% of the melting point of the alloy is the ideal temperature range for sintering of metal powders [13]. This selection is because fine metallic particles possess lower melting points and higher surface energy driving force for binding compared to coarse particles [33, 34]. Besides, small particles might avoid transient liquid state of they have already being dissolved in the solid solution [35]. Thus, the temperature of the second sintering step of 1300 °C (70% of the expected melting point of the Ti–15Mo–5In alloy) was expected to encourage atomic diffusion, which was confirmed by the homogeneous atomic distribution in Fig. 1. Additionally, the temperature was also low enough to avoid large pores formation. It is also expected that the sintering

**Figure 1** a Micrograph of the Ti–15Mo–5In alloy and (b–d) EDS mappings of its constituent elements.



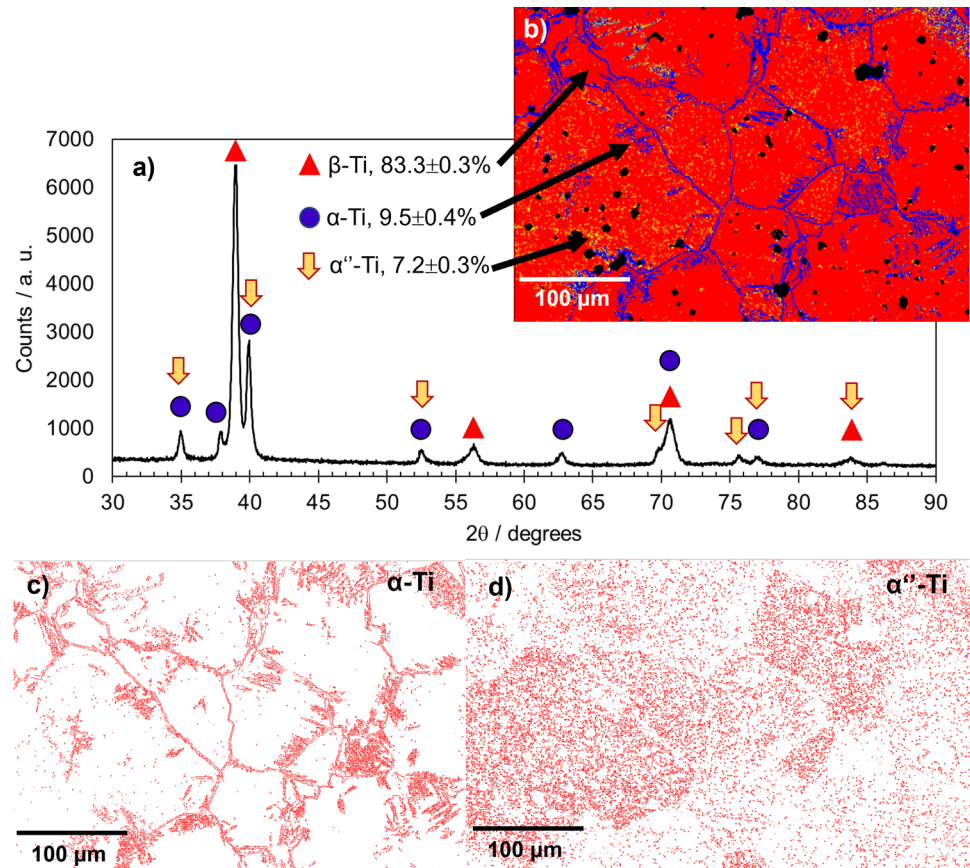
temperature allowed forming strong atomic bonding, which will be evaluated by mechanical properties in Section "Mechanical behavior".

Figure 1 shows micrometric grain sizes, which was congruent with the low porosity and chemical homogeneity. Residual porosity and segregations of elements with low diffusion rate like Mo can restrict grain growth of Ti alloys [35, 36]. The relative density of the Ti–15Mo–5In alloy was  $99.5 \pm 0.1\%$ , which agrees with the low porosity shown in Fig. 1a. From the literature, low percentage porosity can be classified as closed porosity due to the lack of interconnection among the pores [35].

Similar low porosities have been reported for binary Ti–15Mo alloys produced by P&S [26]. Furthermore, the densification could be also influenced by the particle size distribution due to surface diffusion [37] and low melting point of In. Low porosity can be related to the use of fine alloying powders of 4–29  $\mu\text{m}$ . Fine starting powders allow enough atomic diffusion due to shorter diffusion distances and higher surface to volume ratio, which also results in a low quantity of remanent particles in the microstructure [35, 38].

Figure 2 shows the distribution, content, and morphology of the phases in the Ti–15Mo–5In alloy. The morphology of phases corresponds to acicular  $\alpha$  and fine  $\alpha''$  distributed in semi-equiaxed  $\beta$  phase. The phases content agreed with the chemical composition of the alloy. The Mo equivalency ( $\text{Mo}_{\text{eq}}$ ) equals 15 [28, 39], which is higher than the Mo concentration required to retain a single  $\beta$ -Ti phase microstructure in quenched binary Ti–Mo alloys ( $> 10 \text{ wt}\%$ ) [28, 40]. However, the Ti–15Mo–5In alloy also contains In as an alloying element, which was not counted in the Mo equivalency calculation in the literature. Indium contents lower than 20 wt%, which is the case for our Ti–15Mo–5In alloy with 5 wt% In, are expected to form a solid solution [41]. Ti–In alloys form single  $\alpha$ -Ti phase microstructures with In contents up to  $\sim 44 \text{ wt}\%$  by arc-melting [32, 41] and up to 10 wt% In by powder metallurgy [24]. However, some other works suggested a  $\beta$ -stabilizing effect of In additions due to decreasing of the  $\beta$ -critical transformation temperature [32]. Consequently, the effect of In in the equivalencies of  $\beta$ -Ti or  $\alpha$ -Ti stabilizers [39] is not established yet. By comparing our Ti–15Mo–5In alloy with 9.5%  $\alpha$ -phase

**Figure 2** a X-ray diffraction pattern and (b) EBSD phase map of the Ti–15Mo–5In alloy, where  $\beta$ ,  $\alpha$ , and  $\alpha''$  phases correspond to red, blue, and yellow colors, respectively. The (c–d) EBSD maps show the distribution of  $\alpha$  and  $\alpha''$  phases in more detail.



in this study with Ti–15Mo alloys with negligible  $\alpha$ -phase [27, 42–44], it appears that In favors  $\alpha$ -phase formation. However, a systematic study on the effect of In contents on phase stabilization is required to establish this.

From the literature, Mo contents > 4 wt% in binary Ti–Mo alloys are necessary to allow the crystallographic transition from HCP to orthorhombic structure [40]. However, at Mo content of 10 wt%, the  $\beta$ -Ti phase is expected to be stable and the formation of metastable  $\alpha''$ -martensite (orthorhombic) phase is suppressed [40]. Figure 2a shows that even though the Mo content in the Ti–15Mo–5In alloy was higher than the required for suppressing the  $\alpha''$  formation, the phase formation could be affected by the probable  $\alpha$ -stabilizing effect of the In content or the thermomechanical processing of the alloy. The same 5 wt% of In in P&S-processed Ti alloy has shown a dominant  $\alpha$  microstructure with In segregations [24]. Thus, the probable destabilization of  $\beta$  phase would favor the formation of the metastable  $\alpha''$  phase. On the other hand, the low cooling rate from the sintering temperature ( $\sim 15$  °C/min) was expected to favor the formation of equilibrium  $\alpha$  and  $\beta$  phases without the formation of athermal orthorhombic  $\alpha''$  [40]. Formation of  $\alpha''$ -phase is allowed by the correspondence of c-axis between a distorted hexagonal ( $\alpha'$ -martensite phase) and orthorhombic ( $\alpha''$  phase) cells [44]. By comparing Ti–Mo alloys fabricated by P&S with similar Mo contents [26, 45] to the present work, the final phase content is in good agreement. Thus, In may not have a direct effect on  $\beta$  destabilization but on stabilizing hexagonal cells [32].

The formation of  $\alpha''$  phase could be influenced by different factors: (i) strain-induced phase transformation, (ii) the high content of  $\beta$ -stabilizers, or (iii) occurrence of spinodal decomposition. Mechanically applied strains during powders compaction may trigger the formation of metastable  $\alpha''$  phase, which is intermediate during the transformation from  $\beta$  (BCC) to the equilibrium  $\alpha$  (HCP) phase [40]. Besides, strain-induced transformation to form  $\alpha''$  phase requires lower strains than the  $\alpha$  phase [40]. On the other hand, the high contents of Mo as  $\beta$ -stabilizer in the Ti–15Mo–5In alloy could restrict the formation of  $\alpha''$  phase [46], which is shown in Fig. 2. In parallel, the high contents of  $\beta$  stabilizer could limit the formation of equilibrium  $\alpha$  phase. For last, the fine size of the metastable  $\alpha''$  phase agrees well with the spinodal decomposition widely reported in Ti–Mo alloys [31,

47, 48]. The spinodal decomposition has been reported in Ti alloys with more than 4 wt% Mo, which is the case for our alloy. This phenomenon involves the spontaneous separation of a single phase into two distinct phases with different physical properties and chemical concentration fluctuations. For Ti–Mo alloys, the decomposition starts at prior  $\beta$  boundaries and consists of a cellular decomposition of  $\alpha''$  to form metastable Mo-enriched  $\alpha''$  and Mo-depleted  $\alpha$  phases to posteriorly form  $\alpha$  and  $\beta$  phases.  $\alpha$  and  $\beta$  phases nucleate at prior  $\beta$  boundaries consuming the Mo-enriched  $\alpha''$  and Mo-depleted  $\alpha$  phases [47]. Significant hardening effect is commonly obtained after decomposition due to second-phase dispersion effect. Similar phase content has been reported in uniaxially compacted and then sintered Ti–35Nb–5In alloy [49].

More detailed of morphologies and element distribution can be observed in Fig. 3. The acicular and nearly equiaxed morphologies of the  $\alpha$  and  $\beta$  phases are well observed (Fig. 3a, b). Line scans were performed to observe the local distribution of solute in the Ti–15Mo–5In alloy, a representative result is shown in Fig. 3c. As expected, the Mo, which is a strong  $\beta$ -stabilizer with low diffusion in Ti, is mainly found in the micrometric  $\beta$  phase compared to the acicular  $\alpha$  and the finely dispersed  $\alpha''$  (Fig. 3e). The indium showed a nearly constant distribution through the microstructure.

The homogeneous distribution of In in the Ti–15Mo–5In alloy was different from the heterogeneous distribution prevalent in grain boundaries previously reported in porous Ti with 2.5 to 10 wt% In alloys [24]. However, this can be explained by the dominance of  $\alpha$ -Ti phase in the literature, which according to the Ti–In [32] and Ti–Mo [50] diagram phases, allows a lower solubility of In compared to the  $\beta$ -Ti phase predominant in this work.

On the other hand, the fine  $\alpha$  lamella thickness (Fig. 3b) and its distribution mainly near the  $\beta$  grain boundaries is comparable to the reported microstructures of Ti–14Mo and Ti–16Mo alloys [45]. High-energy sites, such as triple junctions, may act as  $\alpha$  phase precipitation sites. This phenomenon may explain the preferred location of  $\alpha$  phase at the  $\beta$  boundaries, which posteriorly could grow towards the inner grain [51]. The  $\alpha$  lamella thickness is controlled by atomic diffusion of Mo in  $\beta$ -Ti [36]. Thus, the  $\alpha$  thickness increases with temperature and decreases with the Mo content. The effect of In in the  $\alpha$  thickness has not been studied. However, considering the low

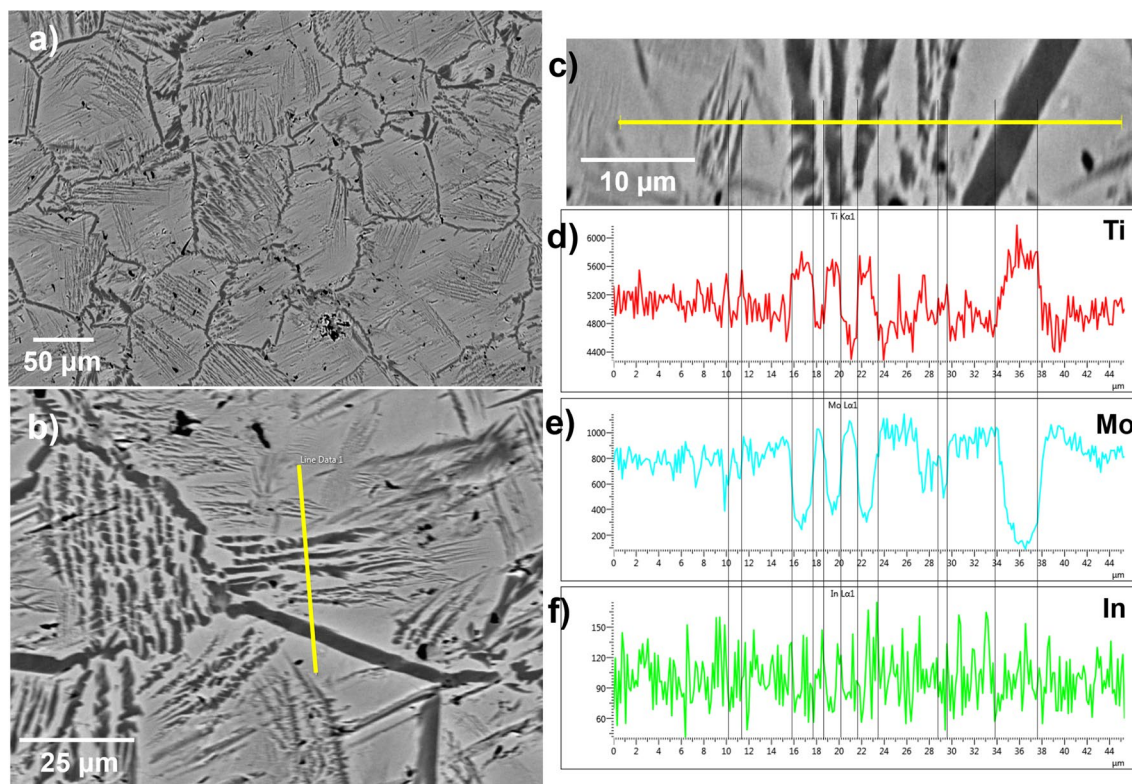


**Figure 3** (a–b) SEM micrographs of the Ti–15Mo–5In alloy and (c–d) line profile distribution of solute elements on the present phases.

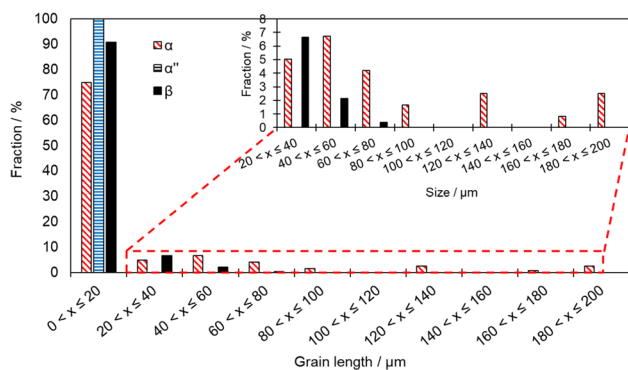


**Figure 4** Grain length distribution on the Ti–15Mo–5In alloy

diffusion coefficient of In in Ti [52], it might have a similar effect than Mo.

Figure 4 shows the distribution of grain length of the present phases obtained from EBSD analyses. Grain length was calculated instead of grain diameter due to the irregular shapes of  $\alpha$  and  $\alpha''$  phases. At least 74% of the three constituent phases range in lengths lower than 20  $\mu\text{m}$ . However, the  $\alpha$  and  $\beta$  phases have visibly broader grain length distribution than the  $\alpha''$  phase.

Comparison with binary Ti–Mo and Ti–In alloys fabricated by P&S from the literature were done to analyse the final  $\alpha$  and  $\beta$  sizes. It was reported that for Ti–14Mo and Ti–16Mo obtained at similar sintering temperatures, the  $\beta$  grain sizes were of  $\sim 40 \mu\text{m}$  [45]. Comparing that size to the grain length distribution in Fig. 4, the  $\beta$  phase of the Ti–15Mo–5In is slightly smaller. This result might be related to the In content, which showed a grain growth pinning effect on a P&S-obtained Ti–5In alloy [24]. The reported pinning effect of In was attributed to its segregation at grain boundaries. Nevertheless, In did not show that behavior at grain boundaries in the Ti–15Mo–5In alloy. Segregations of Mo can also inhibit the grain growth of Ti alloys [35]. However, the representative EDS mapping from Fig. 1 showed an homogeneous distribution of solute elements. Thus, the grain size differences might be related to the different temperature or holding time during sintering in the Ti–Mo alloys from literature [45] compared to those of the present work.

Figure 5 displays the experimental misorientation histograms by correlated (green bars) and uncorrelated (orange bars) distributions of the dominant  $\beta$  (cubic) and  $\alpha$  (hexagonal) phases in the Ti–15Mo–5In

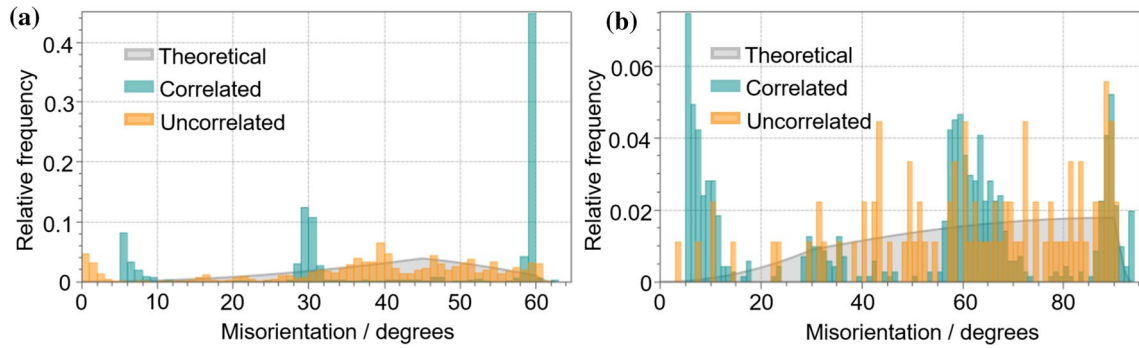


**Figure 5** Comparison of experimental (correlated and uncorrelated) and theoretical uncorrelated misorientation profiles for (a)  $\beta$  and (b)  $\alpha$  phases in the Ti–15Mo–5In alloy.

alloy. For comparison, the theoretical uncorrelated misorientation profiles (gray profiles) for non-preferentially oriented (random crystallographic texture) cubic [53] (Fig. 5a) and hexagonal [54] (Fig. 5b) structures are also shown. Uncorrelated misorientation, also known as texture derivatives profiles, account for all possible misorientations without assuming a spatial correlation between pixels. This means that the measured points are not necessarily contiguous with each other and may even belong to different grains. Thus, uncorrelated profiles may be influenced by transgranular misorientation.

On the other hand, correlated misorientation represents angle comparisons between neighboring points. Considering that the biggest extension corresponds to the inside grain zones, a high frequency of misorientations lower than  $5^\circ$  is commonly observed. Dismissing the expected high frequency misorientations at low angles, the correlated histograms in Fig. 5 were plotted since  $5^\circ$  of misorientation.

From Fig. 5, the uncorrelated misorientation histograms of both  $\alpha$  and  $\beta$  do not agree with the theoretical random profiles. Thus, both phases have preferred crystallographic orientations. The differences between correlated and uncorrelated profiles of  $\beta$  and  $\alpha$  phases suggest significant misorientation disparity between the inner grain and their neighbourhood [55]. Therefore, transgranular strain may be present in the Ti–15Mo–5In alloy, which may be related to the fine  $\alpha''$  phase within the grain or to the twinning commonly activated during the  $\beta$ - $\alpha''$ - $\alpha$  strain-induced phase transformation [56, 57].

The correlated histograms of the  $\beta$  phase (Fig. 5a) showed predominantly high angle grain boundaries (HAGBs), which is congruent with its equilibrium

formation. It is well reported that stable HAGBs possess higher energy compared to low angle grain boundaries (LAGBs) [58]. The high density of  $\beta$  HAGBs assist with precipitation sites for the  $\alpha$  phase [51].

### Mechanical behavior

Flexural and compressive tests were performed in the Ti–15Mo–5In alloy to evaluate its performance under common stress states for biomedical materials. Examples of the above are the compression and flexion stresses exerted between teeth during chewing or joint flexions. The elastic modulus, which is a crucial parameter for the mechanical effectivity of biomedical implants, was also measured. The results are shown in Fig. 6 and Table 1.

The mechanical effectiveness of the new Ti–15Mo–5In alloy should be analyzed in terms of the mechanical behavior of human bone and other Ti alloys reported as feasible for implants. The flexural

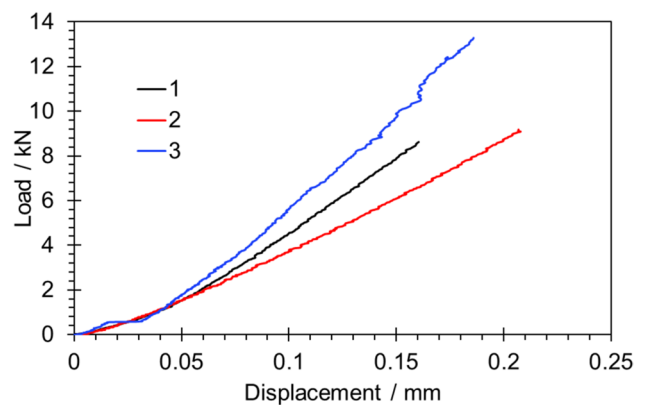


**Figure 6** Four-point flexural results of the Ti–15Mo–5In alloy.



**Table 1** Average of mechanical properties obtained by four-point flexural, ATPC, and hardness tests in the Ti–15Mo–5In alloy

Ultimate flexural strength (MPa)	Flexural displacement to fracture (mm)	Elastic modulus	Microhardness (HV)
595 ± 99	0.18 ± 0.02	80 ± 14	405 ± 55

strength (0.59 GPa) of the Ti–15Mo–5In is superior than that of human bone (0.35–0.39 GPa) [59], as well as that of biomedical Ti–Zr (0.47–0.50 GPa) [60] and Ti–In (~ 0.3 GPa) [24] alloys.

The stiffness mismatch between the implant and the human bone, given by the elastic modulus, should be small to decrease the stress shielding and bone degradation likelihood [4, 5, 8]. Although the Ti–15Mo–5In alloy has a higher elastic modulus (80 GPa) than cortical bone (< 30 GPa) [12], it is lower than various biomedical metallic materials. Examples of biomedical implant alloys with higher elastic modulus than the Ti–15Mo–5In alloy are Ti–6Al–4 V (~ 105 GPa) [61], Ti–Zr (82–115 GPa) [60] and Ti–In (114–117 GPa) [24]. This may be related to the lower elastic moduli well reported in  $\beta$  and predominantly  $\beta$  alloys, such as the Ti–15Mo–5In, compared to those of  $\alpha$  and near- $\alpha$  alloys [26], such as the Ti–Zr, Ti–6Al–4 V, and Ti–In. The elastic modulus (80 GPa) of the new Ti–15Mo–5In alloy was comparable to that of other near- $\beta$ -alloys, such as Ti–Nb–Mo (64–96 GPa) [30] and Ti–35Nb–5In alloys [49].

The average hardness (~ 3.9 GPa) of the Ti–15Mo–5In alloy was higher than that of different bone regions, such as osteonal, trabecular, and interstitial, ranging between 0.23 and 0.76 GPa [7]. It was also higher than the hardness of various biomedical Ti alloys, such as Ti–In (1.3–1.4 GPa) [24], Ti–6Al–4 V (~ 2.8 GPa) [61], and Ti–Nb–Mo alloys (1.8–2.8 GPa) [30].

The microstructural characteristics of the Ti–15Mo–5In alloy strongly influenced its good

mechanical properties. Binary Ti–Mo alloys [45] have been reported with similar morphology and phases content to the Ti–15Mo–5In of this work. As explained from Fig. 4, the grain sizes of the Ti–Mo alloys were reported slightly higher than that of the Ti–15Mo–5In alloy. However, the microhardness of Ti–Mo alloys (337–403 HV) was slightly lower than that of the Ti–15Mo–5In alloy (405 HV). This was not expected since the  $\beta$ -Ti phase is dominant in both systems and it tends to increase hardness with increasing the grain size [62]. This contrasting result may be related to the combined effect of Mo and In as alloying elements, and specially due to their adequate content. From the binary P&S-elaborated Ti–Mo [45] and Ti–In [24] systems, contents of 16 wt% of Mo and 5 wt% of In obtained the highest hardness compared to other Mo and In contents. The hardness of the Ti–15Mo–5In alloy might be enhanced by the second-phase dispersion effect triggered by the spinodal decomposition described in Section "Microstructural characterization". Because of this, Ti–15Mo–5In alloy in this study showed significantly higher hardness (~ 3.9 GPa) than Ti–15Mo and Ti–15Mo–2In alloys without reported  $\alpha''$  phase (~ 0.9 to 1.3 GPa) [63]. From the above, the Ti–15Mo–5In alloy is feasible in terms of mechanical properties for use in biomedical implant applications.

### Ion release and electrochemical evaluations

Ensuring metal ion release rates below harmful levels is essential for the low toxicity of biomedical implants, so they can be introduced into in vivo systems, such as the human body. Metallic ions can diffuse and accumulate into the human body and cause allergy and carcinoma at large concentrations [64]. Thus, a reliable implant material must have ion release rates lower than the reported toxicity levels or the recommended dietary intake.

Table 2 shows the ion release from the Ti–15Mo–5In alloy, which were lower than the toxic concentrations for human health. The  $\text{Ti}^{3+}$  ion release was well below the concentrations that inhibit and do not stimulate

**Table 2** Average metal ion release from the Ti–15Mo–5In alloy and corrosion rate after immersion in modified Ringer-Hartmann artificial saliva

Ion release rate ( $\mu\text{g L}^{-1} \text{cm}^{-2} \text{h}^{-1}$ )			Corrosion rate ( $\text{mg dm}^{-2} \text{day}^{-1}$ )	Corrosion rate ( $\mu\text{m year}^{-1}$ )
Ti	Mo	In		
0.019 ± 0.009	0.622 ± 0.421	0.001 ± 0.09	0.078 ± 0.052	0.524 ± 0.113

cell proliferation, i.e., 10 ppm ( $10000 \mu\text{g L}^{-1}$ ) and 5 ppm ( $5000 \mu\text{g L}^{-1}$ ) [65]. Likewise, the In release was lower than the concentration that causes 50% of L-929 fibroblasts death, i.e.,  $2310 \mu\text{M}$  ( $2.65 \times 10^5 \mu\text{g L}^{-1}$ ) [40]. In release was also within the nontoxic limit of 50 ppm ( $50000 \mu\text{g L}^{-1}$ ) [66]. The Mo ion release rates indicate up to  $14.9 \mu\text{g L}^{-1}$  per day from a  $1 \text{ cm}^2$  implant. That ion release is within the recommended dietary allowance of Mo from 17 to  $45 \mu\text{g day}^{-1}$  for children and adult people [67], which indicate a low toxicity likelihood for humans. Therefore, the Ti–15Mo–5In alloy did not show potential toxicity to human health due to its metal ion release rates.

Due to the scarce information on the Ti–Mo–In system in the literature, comparisons were made with other P&S-processed alloys with similar relative density ( $>93\%$ ) tested under similar conditions. The Fig. 7a shows the advantages of Ti–15Mo–5In alloy compared to other reported alloys for implants. Lower concentrations of Ti and In were released from the Ti–15Mo–5In alloy compared to other reported systems. While ion Mo release was within the Mo release range of the Ti–Nb–Mo alloys. Considering that both Ti–Nb–Mo and Ti–In systems were considered as feasible for biomedical implants [24, 30], it can be expected the same for the Ti–15Mo–5In alloy.

On the other hand, the average corrosion rate measured after artificial saliva immersion of the

Ti–15Mo–5In alloy ( $0.078 \text{ mg dm}^{-2} \text{ day}^{-1}$ ) was well below the corrosion rates reported for P&S-processed Ti–Nb–Mo alloys with different Nb and Mo contents and surface laser treatments [30]. The corrosion rate after immersion in artificial saliva was not reported for the Ti–In alloys from the literature. However, better corrosion resistance of the Ti–15Mo–5In alloy respect to the Ti–In alloys was suggested by the lower ion released rates in Fig. 7a and by the lower microstructural attack after testing (Fig. 7b). The Ti–In alloys, including the Ti–5In from the literature showed high preferred corrosion at the grain boundaries [24], while no visible corrosion can be observed in the Ti–15Mo–5In alloy (Fig. 7b) after similar testing conditions. Similar high corrosion attack was showed for the Ti–Nb–Mo from the literature [30]. It is worth mentioning that the Ti–15Mo–5In alloy did not show cracking or pitting corrosion by the corrosive environment.

Factors that influence the corrosion resistance of alloys elaborated by P&S include porosity, chemical heterogeneities, grain size, phase content, and chemical composition. The Ti–15Mo–5In showed a homogeneous distribution of alloying elements (Fig. 1) and similar relative density ( $99.5\%$ ) than Ti–Nb–Mo ( $>93\%$ ) and Ti–In ( $>98\%$ ) alloys. Regarding grain size, the Ti–5In alloy showed a broad grain size ranging from 50 to  $150 \mu\text{m}$  [24], the Ti–Nb–Mo alloys from 13 to  $47 \mu\text{m}$  [30], and from Fig. 4, the Ti–15Mo–5In of this

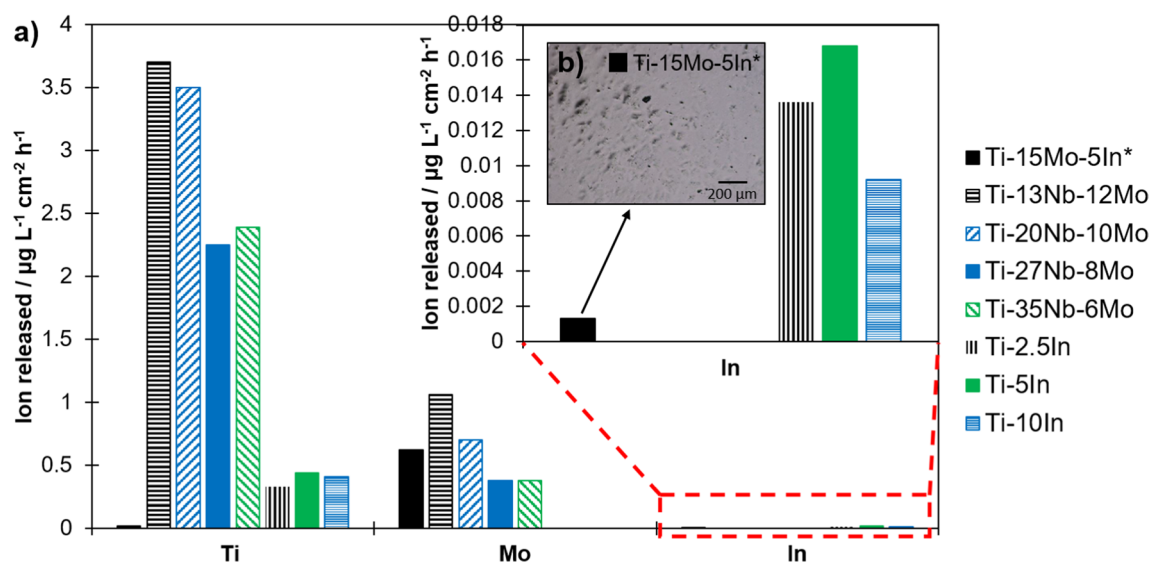


**Figure 7** (a) Comparison of ion release between the Ti–15Mo–5In (\*this work) and other reported porous Ti–In [24] elaborated by P&S, Ti–Nb–Mo [30] elaborated by P&S and laser surface treatment at 1000 W. All the alloys were tested at  $37 \text{ }^\circ\text{C}$  for 730 h

in artificial saliva with pH between 5.2 and 6.5. (b) Superficial attack on the Ti–15Mo–5In alloy after immersion in artificial saliva.

work has 90% grain sizes below 20  $\mu\text{m}$ . Lower grain size may be advantageous in promoting a more compacted and adherent passive oxide layer compared to coarse-grained microstructures [68]. This is because fine grain sizes increase the electronic activity near grain limits, increasing the surface reactivity to form oxide layers. Besides, grain boundaries may serve as nucleation sites for passive layer formation, improving its formation kinetics, coherency, adherence and stability [68]. However, the Ti–15Mo–5In of this work revealed a lower corrosion rate ( $0.078 \text{ mg dm}^{-2} \text{ day}^{-1}$ ) than the reported Ti–35Nb–6Mo alloy with lower average grain size of 16.21  $\mu\text{m}$  [30]. Therefore, parameters other than grain size, such as phases percentage and chemical composition, may have a strong influence on the corrosion behavior of the Ti–15Mo–5In alloy.

The Ti–15Mo–5In alloy with 78.5% of  $\beta$  phase will be compared to the Ti–Nb–Mo (processed at 1000 W) with more than 94% of  $\beta$  phase, and the Ti–5In alloy with 100% of  $\alpha$  phase and In segregations. It has been reported that the  $\beta$ -Ti phase and  $\alpha/\beta$  interfaces are preferred dissolution sites at HCl and artificial saliva media [61, 69]. Thus, single phase Ti alloys might be preferred for boosting the corrosion performance. Nevertheless, the near single  $\alpha$  and  $\beta$  phases alloys immersed in artificial saliva reported higher corrosion susceptibility than the tri-phasic microstructure of the Ti–15Mo–5In alloy. This tendency, contrary to the reported from the literature, may indicate a strong influence of the combined effect of In and Mo.

Indium can decrease the corrosion susceptibility of metallic materials [70], including Ti alloys [24]. Other work reported a similar corrosion resistance between Ti–In alloys and pure Ti [41]. Mo is also well known for improving the corrosion resistance of Ti alloys [9] respect to CP–Ti. It can be expected the Mo and In acted synergistically to decrease the corrosion susceptibility of the Ti–15Mo–5In alloy. Corrosion susceptibility measured under electrochemical conditions is necessary to deeply understand the corrosion performance of the new Ti–15Mo–5In alloy.

The OCP, polarization graphs, and average corrosion parameters after electrochemical testing of the Ti–15Mo–5In are displayed in Fig. 8. The negative OCP values from Fig. 8a (average of  $-0.25 \pm \text{V}$ ) indicate an active metal ground base. The potential increased in the primary immersion stage up to  $< 1000$  s. After 1000 s, the potential remained almost constant, which indicates the formation of surface passive layer. Besides, less negative OCP values suggest

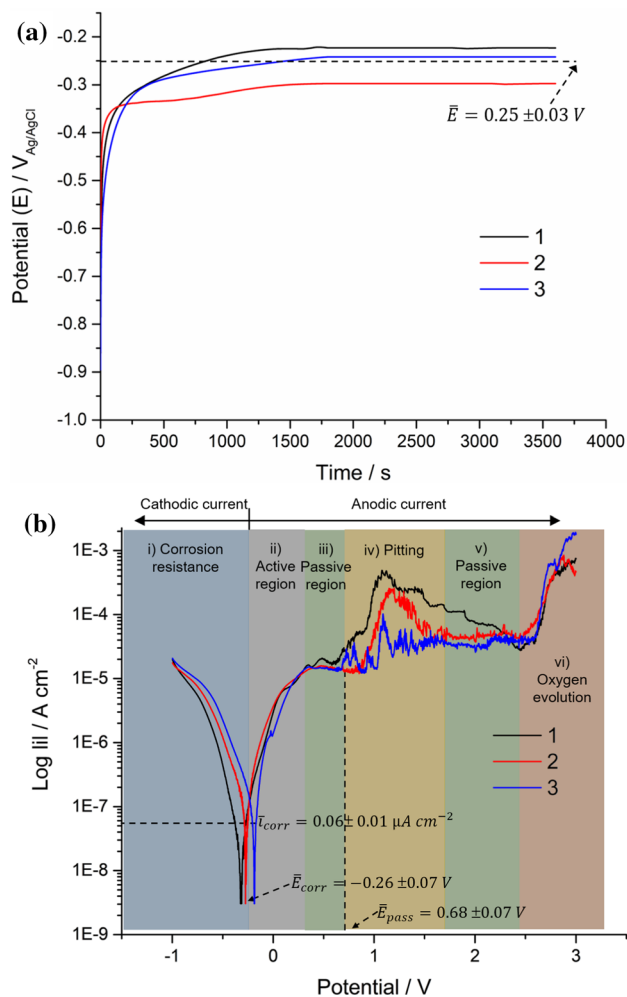


**Figure 8** (a) OCP and (b) PD polarization curves for the Ti–15Mo–5In alloy. Three repetitions are shown for statistical purposes.

the formation of more compacted and adhered passive layer. The OCP values measured for the Ti–15Mo–5In alloy were less negative than those reported for P&S-processed Ti–In alloys and Ti–34Nb–6Sn compacted at 200 MPa [21, 24], additive manufactured Ti–6Al–4 V [61], densified Ti–6Al–4 V ELI, Ti–13Mo–7Zr–3Fe (TMZF), Ti–35Nb–7Zr–5Ta [69], and Ti–6Al–4 V with TiAlN/TiAlCrN coating [71].

The three measurements of potentiodynamic (PD) polarization curves in the Ti–15Mo–5In alloy are shown in Fig. 8b. The polarization behavior can be described by five regions; (i) cathodic behavior and corrosion resistance, (ii) general corrosion and anodic behavior, (iii) formation of surface passive layer, (iv) localized corrosion resulted from ionic electrolyte infiltration through the passive film, (v) regeneration of

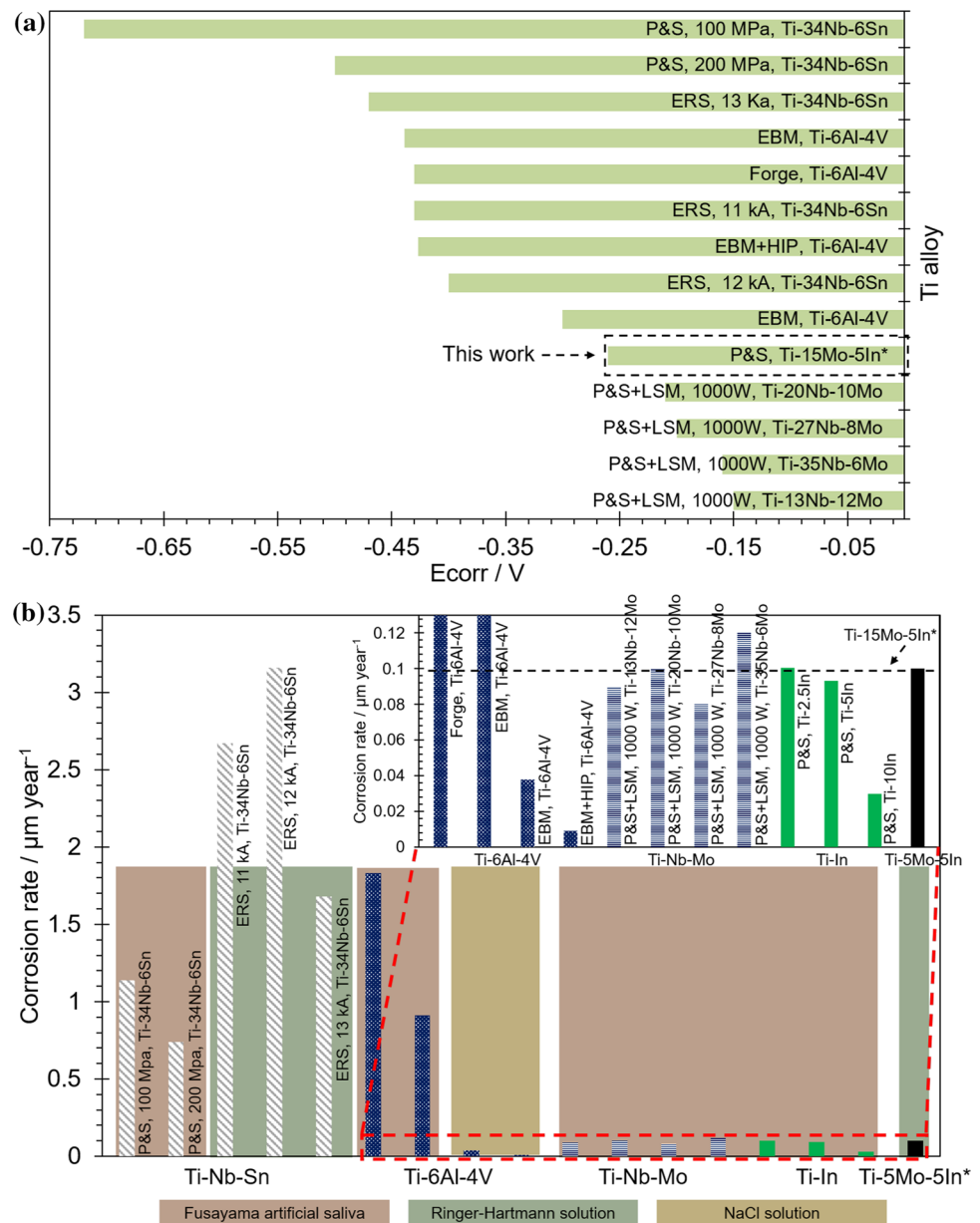
surface passive film, (vi) molecular oxygen evolution from the overall electrochemical reaction.

The three polarization curves show a good reproducibility with average corrosion potential ( $E_{\text{corr}}$ ) and current density ( $I_{\text{corr}}$ ) of  $-0.26 \pm 0.07$  V and  $0.06 \pm 0.01 \mu\text{A cm}^{-2}$ . The  $E_{\text{corr}}$  of the Ti-15Mo-5In alloy, which is less negative than that reported for Ti-6Al-4V and Ti-Nb-Sn alloys (Fig. 9a), indicates the lower electrochemical activity of the former due to a more stable passive layer.

The average corrosion rate of the Ti-15Mo-5In alloy ( $0.1 \mu\text{m year}^{-1}$ ) was compared to other reported

Ti alloys designed for biomedical implant applications (Fig. 9b). The Ti-15Mo-5In alloy showed less susceptibility to corrosion than the Ti-Nb-Sn system and similar to the Ti-Nb-Mo and Ti-In alloys. It is remarkable that despite the different thermo-mechanical histories of the compared alloys, the electrochemical behavior of the Ti-Nb-Mo, Ti-In, and Ti-15Mo-5In alloys is similar. It has been reported that the microstructure is not always a dominant factor over chemical composition or oxide film effectiveness to define the electrochemical corrosion of Ti alloys [69].

**Figure 9** Comparison of (a)  $E_{\text{corr}}$  and (b) corrosion rate among the Ti-15Mo-5In alloy (this work \*) and reported Ti alloys elaborated by different routes, such as P&S [21, 24], electrical resistance sintering (ERS) [22], forge [61], electron-beam melting (EBM) [61, 74], P&S + surface laser treatment (LSM) [30], and EBM + hot isostatic pressing (HIP) [74] in different corrosive media (Fusayama, Ringer-Hartmann, or NaCl solutions).



From the above, Ti–15Mo–5In has been shown to have electrochemical performance comparable to or superior to various reported biomedical Ti alloys. Furthermore, the corrosion rate of the Ti–15Mo–5In alloy ( $0.1 \mu\text{m year}^{-1}$ ) can be considered as perfectly stable [72]. The electrochemical behavior of the Ti–15Mo–5In may promote promising key qualities for implants, such as osteointegration and biocompatibility [73]. However, *in vivo* tests are recommended to ensure those qualities.

## Conclusions

The mechanical properties, ion release, and electrochemical assessments were uncovered and analyzed with respect to the microstructural condition of the new porous Ti–15Mo–5In alloy. Based on the following findings, the Ti–15Mo–5In met mechanical, toxicity, and corrosion criteria for orthopedic and dental implant candidates:

1. Ti–15Mo–5In alloy was constituted by nearly equiaxed and micrometric  $\beta$  matrix with acicular  $\alpha$  and fine dispersed  $\alpha''$  phases. The misorientation profiles suggested preferred crystallographic orientation on the  $\beta$  and  $\alpha$  phases. By comparing the studied alloy with the literature, the 5 wt% In content seems to favor the  $\alpha$ -phase formation. However, a systematic study on the phase stabilization effect of In is warranted.
2. The hardness (3.9 GPa) and flexural strength (0.59 GPa) of the Ti–15Mo–5In alloy were higher than those reported for human bone. The elastic modulus of the Ti–15Mo–5In alloy (80 GPa) was lower than that of other reported biomedical Ti alloys, but at least 2.7 times higher than that reported for human cortical bone.
3. Ti ( $0.019 \mu\text{gL}^{-1} \text{cm}^{-2} \text{h}^{-1}$ ), Mo ( $0.622 \mu\text{gL}^{-1} \text{cm}^{-2} \text{h}^{-1}$ ), and In ( $0.001 \mu\text{gL}^{-1} \text{cm}^{-2} \text{h}^{-1}$ ) ion releases were below harmful concentrations to human health. The corrosion rates during immersion and electrochemical tests ( $0.524$  and  $0.1 \mu\text{m year}^{-1}$ , respectively) were lower than various reported biomedical alloys. The corrosion behavior was strongly influenced by chemical composition of the alloy, as well as by a continuous formation and regeneration (after pitting) of the surface passive layer.

## Acknowledgements

L.R.R. acknowledges the funding from the Programa de Apoyo a la Investigación y el Posgrado (PAIP-50009223) of the Chemistry College of Universidad Nacional Autónoma de México. M.C.R. acknowledges for the financial support from São Paulo Research Foundation (FAPESP) through “Projeto Temático” # 2018/18293-8, post doc Grant # 2021/03865-9. V. A. B acknowledges the funding from the Spanish Ministerio de Ciencia, Innovación y Universidades with project RTI2018-097810-B-I00, and the European Commission via Fondo Europeo de Desarrollo Regional (FEDER).

## Author contributions

LRR contributed to writing-original draft and visualization. MCR contributed to draft edition and visualization. CSE contributed to methodology and validation. VAB contributed to resources, project administration, and funding acquisition.

## Data availability

The raw data related to this manuscript would be made available on request.

## Declarations

**Conflict of interest** The authors declare that there are no conflicts of interest.

**Ethical approval** Not applicable.

**Open Access** This article is licensed under a Creative Commons Attribution 4.0 International License, which permits use, sharing, adaptation, distribution and reproduction in any medium or format, as long as you give appropriate credit to the original author(s) and the source, provide a link to the Creative Commons licence, and indicate if changes were made. The images or other third party material in this article are included in the article’s Creative Commons licence, unless indicated otherwise in a credit line to the material. If material is not included in the article’s

Creative Commons licence and your intended use is not permitted by statutory regulation or exceeds the permitted use, you will need to obtain permission directly from the copyright holder. To view a copy of this licence, visit <http://creativecommons.org/licenses/by/4.0/>.

## References

- [1] Klug A, Gramlich Y, Rudert M et al (2021) The projected volume of primary and revision total knee arthroplasty will place an immense burden on future health care systems over the next 30 years. *Knee Surgery Sport Traumatol Arthrosc* 29:3287–3298. <https://doi.org/10.1007/s00167-020-06154-7>
- [2] Kurtz S, Ong K, Lau E et al (2007) Projections of primary and revision hip and knee arthroplasty in the United States from 2005 to 2030. *J Bone Jt Surg Ser A* 89:780–785. <https://doi.org/10.2106/JBJS.F.00222>
- [3] Elani HW, Starr JR, Da Silva JD, Gallucci GO (2018) Trends in dental implant use in the U.S., 1999–2016, and projections to 2026. *J Dent Res* 97:1424–1430. <https://doi.org/10.1177/0022034518792567>
- [4] Geetha M, Singh AK, Asokamani R, Gogia AK (2009) Ti based biomaterials, the ultimate choice for orthopaedic implants—a review. *Prog Mater Sci* 54:397–425. <https://doi.org/10.1016/j.pmatsci.2008.06.004>
- [5] Gratton A, Buford B, Goswami T et al (2011) Failure modes of biomedical implants. *J Mech Behav Mater* 13:297–314. <https://doi.org/10.1515/jmbm.2002.13.5-6.297>
- [6] Goia TS, Violin KB, Yoshimoto M et al (2010) Osseointegration of titanium alloy macroporous implants obtained by PM with addition of gelatin. *Adv Sci Technol* 76:259–263. <https://doi.org/10.4028/www.scientific.net/ast.76.259>
- [7] Zysset PK, Guo XE, Ho CE et al (1999) Elastic modulus and hardness of cortical and trabecular bone lamellae measured by nanoindentation in the human femur. *J Biomech* 32:1005–1012. [https://doi.org/10.1016/S0021-9290\(99\)00111-6](https://doi.org/10.1016/S0021-9290(99)00111-6)
- [8] Bram Dr M, Ebel Dr T, Wolff M et al (2013) Applications of powder metallurgy in biomaterials. In: *Advances in powder metallurgy*. Woodhead Publishing, pp 520–554
- [9] Xu W et al (2018) Effects of Porosity on mechanical properties and corrosion resistances of PM-fabricated porous Ti–10Mo alloy. *Metals (Basel)* 8:188–201. <https://doi.org/10.3390/met8030188>
- [10] Pałka K, Pokrowiecki R (2018) Porous titanium implants: a review. *Adv Eng Mater* 20:1700648–1700666. <https://doi.org/10.1002/adem.201700648>
- [11] Dewidar MM, Yoon HC, Lim JK (2006) Mechanical properties of metals for biomedical applications using powder metallurgy process: a review. *Met Mater Int* 12:193–206. <https://doi.org/10.1007/BF03027531>
- [12] Ryan G, Pandit A, Apatsidis DP (2006) Fabrication methods of porous metals for use in orthopaedic applications. *Biomaterials* 27:2651–2670. <https://doi.org/10.1016/j.biomaterials.2005.12.002>
- [13] Committee AIH (1998) Powder metal technologies and applications. ASM International Handbook Committee
- [14] Rossi MC, Resendiz LR, Vicente Amigó Borrás (2022) Magnesium in Synthesis of Porous and Biofunctionalized Metallic Materials. In: *Intechopen*. pp 1–22
- [15] Prasad S, Ehrensberger M, Gibson MP et al (2015) Bio-material properties of titanium in dentistry. *J Oral Biosci* 57:192–199. <https://doi.org/10.1016/j.job.2015.08.001>
- [16] Gosavi S, Gosavi S, Alla R (2013) Titanium: a miracle metal in dentistry. *Trends Biomater Artif Organs* 27:42–46
- [17] Kolamroudi MK, Asmael M, Ilkan M, Kordani N (2021) Developments on electron beam melting (EBM) of Ti–6Al–4V: a review. *Trans Indian Inst Met* 74:783–790. <https://doi.org/10.1007/s12666-021-02230-9>
- [18] Mirza A, King A, Troakes C, Exley C (2017) Aluminium in brain tissue in familial Alzheimer’s disease. *J Trace Elem Med Biol* 40:30–36. <https://doi.org/10.1016/j.jtemb.2016.12.001>
- [19] Catalani S, Stea S, Beraudi A et al (2013) Vanadium release in whole blood, serum and urine of patients implanted with a titanium alloy hip prosthesis. *Clin Toxicol* 51:550–556. <https://doi.org/10.3109/15563650.2013.818682>
- [20] Çaha I, Alves A, Chirico C et al (2020) Corrosion and tribocorrosion behavior of Ti–40Nb and Ti–25Nb–5Fe alloys processed by powder metallurgy. *Metall Mater Trans A Phys Metall Mater Sci* 51:3256–3267. <https://doi.org/10.1007/s11661-020-05757-6>
- [21] Correa-Rossi M, Romero-Resendiz L, Leal-Bayerlein D et al (2022) Mechanical, corrosion, and ion release studies of Ti–34Nb–6Sn alloy with comparable to the bone elastic modulus by powder metallurgy method. *Powders* 1:3–17. <https://doi.org/10.3390/powders1010002>
- [22] Rossi MC, de Santi GE, Rodríguez MVH et al (2021) Study of the current density of the electrical resistance sintering technique on microstructural and mechanical properties in a  $\beta$  Ti–Nb–Sn ternary alloy. *Appl Phys A Mater Sci Process* 127:1–19. <https://doi.org/10.1007/s00339-021-04937-4>

- [23] Rossi MC, Bayerlein DL, Gouvêa EDS et al (2021) Evaluation of the influence of low Mg content on the mechanical and microstructural properties of  $\beta$  titanium alloy. *J Mater Res Technol* 10:916–925. <https://doi.org/10.1016/j.jmrt.2020.12.103>
- [24] Romero-Resendiz L, Gómez-Sáez P, Vicente-Escuder A, Amigó-Borrás V (2021) Development of Ti–In alloys by powder metallurgy for application as dental biomaterial. *J Mater Res Technol* 11:1719–1729. <https://doi.org/10.1016/j.jmrt.2021.02.014>
- [25] Xu W, Liu Z, Lu X et al (2019) Porous Ti–10Mo alloy fabricated by powder metallurgy for promoting bone regeneration. *Sci China Mater* 62:1053–1064. <https://doi.org/10.1007/s40843-018-9394-9>
- [26] Mohan P, Rajak DK, Pruncu CI et al (2021) Influence of  $\beta$ -phase stability in elemental blended Ti–Mo and Ti–Mo–Zr alloys. *Micron* 142:102992–102998. <https://doi.org/10.1016/j.micron.2020.102992>
- [27] Martins JRS, Nogueira RA, De Araújo RO et al (2011) Preparation and characterization of Ti–15Mo alloy used as biomaterial. *Mater Res* 14:107–112. <https://doi.org/10.1590/S1516-14392011005000013>
- [28] Kolli RP, Devaraj A (2018) A review of metastable beta titanium alloys. *Metals (Basel)* 8:1–41. <https://doi.org/10.3390/met8070506>
- [29] Radovic M, Lara-Curzio E, Riestler L (2004) Comparison of different experimental techniques for determination of elastic properties of solids. *Mater Sci Eng A* 368:56–70. <https://doi.org/10.1016/j.msea.2003.09.080>
- [30] Tendero I, Rossi MC, Viera M et al (2021) Laser surface modification in Ti– $x$ Nb– $y$ Mo alloys prepared by powder metallurgy. *Metals (Basel)* 11:367–387. <https://doi.org/10.3390/met11020367>
- [31] Murray JL (1981) The Mo–Ti (Molybdenum–Titanium) system. *Bull Alloy Phase Diagrams* 2:185–192. <https://doi.org/10.1007/BF02881476>
- [32] Gulay LD, Schuster JC (2003) Investigation of the titanium–indium system. *J Alloys Compd* 360:137–142. [https://doi.org/10.1016/S0925-8388\(03\)00319-0](https://doi.org/10.1016/S0925-8388(03)00319-0)
- [33] Allen GL, Bayles RA, Gile WW, Jesser WA (1986) Small particle melting of pure metals. *Thin Solid Films* 144:297–308. [https://doi.org/10.1016/0040-6090\(86\)90422-0](https://doi.org/10.1016/0040-6090(86)90422-0)
- [34] Apai G, Hamilton JF, Stohr J, Thompson A (1979) Extended x-ray absorption fine structure of small Cu and Ni clusters: Binding-energy and bond-length changes with cluster size. *Phys Rev Lett* 43:165–169. <https://doi.org/10.1103/PhysRevLett.43.165>
- [35] Robertson IM, Schaffer GB (2010) Review of densification of titanium based powder systems in press and sinter processing. *Powder Metall* 53:146–162. <https://doi.org/10.1179/174329009X434293>
- [36] Liu Y, Wei WF, Zhou KC et al (2003) Microstructures and mechanical behavior of PM Ti–Mo alloy. *J Cent South Univ Technol (Engl Ed)* 10:81–86. <https://doi.org/10.1007/s11771-003-0043-5>
- [37] Getman OI (2019) Application of skorokhod’s rheological theory of sintering to analyze the sintering kinetics of tungsten powders. *Powder Metall Met Ceram* 58:373–398. <https://doi.org/10.1007/s11106-019-00088-7>
- [38] Ivasishin OM, Eylon D, Bondarchuk VI, Savvakina DG (2008) Diffusion during powder metallurgy synthesis of titanium alloys. *Defect Diffus Forum* 277:177–185. <https://doi.org/10.4028/www.scientific.net/ddf.277.177>
- [39] Chen L, Cui Y, Zhang L (2020) Recent development in beta titanium alloys for biomedical applications. *Metals (Basel)* 10:1139–1168. <https://doi.org/10.3390/met10091139>
- [40] Davis R, Flower HM, West DRF (1979) Martensitic transformations in Ti–Mo alloys. *J Mater Sci* 14:712–722. <https://doi.org/10.1007/BF00772735>
- [41] Han MK, Im JB, Hwang MJ et al (2015) Effect of indium content on the microstructure, mechanical properties and corrosion behavior of titanium alloys. *Metals (Basel)* 5:850–862. <https://doi.org/10.3390/met5020850>
- [42] Nag S, Banerjee R, Fraser HL (2005) Microstructural evolution and strengthening mechanisms in Ti–Nb–Zr–Ta, Ti–Mo–Zr–Fe and Ti–15Mo biocompatible alloys. *Mater Sci Eng C* 25:357–362. <https://doi.org/10.1016/j.msec.2004.12.013>
- [43] Kumar S, Narayanan TSNS (2008) Corrosion behaviour of Ti–15Mo alloy for dental implant applications. *J Dent* 36:500–507. <https://doi.org/10.1016/j.jdent.2008.03.007>
- [44] Ho W-F (2008) A comparison of tensile properties and corrosion behavior of cast Ti–7.5Mo with c.p. Ti, Ti–15Mo and Ti–6Al–4V alloys. *J Alloys Compd* 464:580–583. <https://doi.org/10.1016/j.jallcom.2007.10.054>
- [45] Xu W, Chen M, Lu X et al (2020) Effects of Mo content on corrosion and tribocorrosion behaviours of Ti–Mo orthopaedic alloys fabricated by powder metallurgy. *Corros Sci* 168:108557–108567. <https://doi.org/10.1016/j.corsci.2020.108557>
- [46] Banerjee S, Mukhopadhyay P (2007) Phase transformations: examples from titanium and zirconium alloys. Elsevier, Amsterdam
- [47] Davis R, Flower HM, West DRF (1979) The decomposition of Ti–Mo alloy martensites by nucleation and growth and spinodal mechanisms. *Acta Metall* 27:1041–1052. [https://doi.org/10.1016/0001-6160\(79\)90192-5](https://doi.org/10.1016/0001-6160(79)90192-5)
- [48] George A, Divakar R (2019) Evidence for spinodal decomposition in Ti–15Mo quenched alloy using transmission

- electron microscopy. *Micron* 121:43–52. <https://doi.org/10.1016/j.micron.2019.03.003>
- [49] Romero-Resendiz L, Rossi MC, Segui-Esquembre C, Amigo-Borrás V (2023) Development of a porous Ti–35Nb–5In alloy with low elastic modulus for biomedical implants. *J Mater Res Technol* 22:1151–1164. <https://doi.org/10.1016/j.jmrt.2022.12.011>
- [50] The Materials Information Society (1992) *ASM Handbook - Alloy Phase Diagrams*
- [51] Salib M, Teixeira J, Germain L et al (2013) Influence of transformation temperature on microtexture formation associated with  $\alpha$  precipitation at  $\beta$  grain boundaries in a  $\beta$  metastable titanium alloy. *ACTA Mater* 61:3758–3768. <https://doi.org/10.1016/j.actamat.2013.03.007>
- [52] Pérez RA, Soares MRF, Behar M, Dymont F (1997) Indium diffusion study in  $\alpha$ -titanium. *J Nucl Mater* 249:52–57. [https://doi.org/10.1016/S0022-3115\(97\)00181-5](https://doi.org/10.1016/S0022-3115(97)00181-5)
- [53] Mackenzie JK (1958) Second paper on statistics associated with the random disorientation of cubes. *Biometrika* 45:229–240. <https://doi.org/10.2307/2333253>
- [54] Hu Y, Randle V (2007) An electron backscatter diffraction analysis of misorientation distributions in titanium alloys. *Scr Mater* 56:1051–1054. <https://doi.org/10.1016/j.scripamat.2007.02.030>
- [55] Romero-Resendiz L, Cabrera JM, Elizalde S et al (2022) Mechanical, stress corrosion cracking and crystallographic study on flat components processed by two combined severe plastic deformation techniques. *J Mater Res Technol* 18:1281–1294. <https://doi.org/10.1016/j.jmrt.2022.03.010>
- [56] Ji X, Gutierrez-Urrutia I, Emura S et al (2019) Twinning behavior of orthorhombic- $\alpha''$  martensite in a Ti–7.5Mo alloy. *Sci Technol Adv Mater* 20:401–411. <https://doi.org/10.1080/14686996.2019.1600201>
- [57] Li C, Li G, Yang Y et al (2011) Martensitic twinning in Alpha + Beta Ti–3.5Al–4.5Mo titanium alloy. *J Metall* 2011:1–5. <https://doi.org/10.1155/2011/924032>
- [58] Rohrer GS (2016) The role of grain boundary energy in grain boundary complexion transitions. *Curr Opin Solid State Mater Sci* 20:231–239. <https://doi.org/10.1016/j.cossms.2016.03.001>
- [59] Rho JY, Kuhn-Spearing L, Zioupos P (1998) Mechanical properties and the hierarchical structure of bone. *Med Eng Phys* 20:92–102. [https://doi.org/10.1016/S1350-4533\(98\)00007-1](https://doi.org/10.1016/S1350-4533(98)00007-1)
- [60] Amigó-Mata A, Haro-Rodríguez M, Vicente-Escuder Á, Amigó-Borrás V (2022) Development of Ti–Zr alloys by powder metallurgy for biomedical applications. *Powder Metall* 65:31–38. <https://doi.org/10.1080/00325899.2021.1943182>
- [61] Romero-Resendiz L, Rossi MC, Alvarez A et al (2022) Microstructural, mechanical, electrochemical, and biological studies of an electron beam melted Ti–6Al–4V alloy. *Mater Today Commun* 31:103337–103351. <https://doi.org/10.1016/j.mtcomm.2022.103337>
- [62] Kao YL, Tu GC, Huang CA, Liu TT (2005) A study on the hardness variation of  $\alpha$ - and  $\beta$ -pure titanium with different grain sizes. *Mater Sci Eng A* 398:93–98. <https://doi.org/10.1016/j.msea.2005.03.004>
- [63] Al-Murshdy JMS, Al-Deen HHJ, Hussein SR (2021) Investigation of the effect of indium addition on the mechanical and electrochemical properties of the Ti–15Mo biomedical alloy. *J Bio Tribo Corrosion* 7:1–18. <https://doi.org/10.1007/s40735-021-00581-w>
- [64] Hanawa T (2004) Metal ion release from metal implants. *Mater Sci Eng C* 24:745–752. <https://doi.org/10.1016/j.msec.2004.08.018>
- [65] Liao H, Wurtz T, Li J (1999) Influence of titanium ion on mineral formation and properties of osteoid nodules in rat calvaria cultures. *J Biomed Mater Res* 47:220–227. [https://doi.org/10.1002/\(SICI\)1097-4636\(199911\)47:2%3c220::AID-JBM12%3e3.0.CO;2-9](https://doi.org/10.1002/(SICI)1097-4636(199911)47:2%3c220::AID-JBM12%3e3.0.CO;2-9)
- [66] Wataha JC, Hanks CT, Craig RG (1991) The in vitro effects of metal cations on eukaryotic cell metabolism. *J Biomed Mater Res* 25:1133–1149. <https://doi.org/10.1002/jbm.820250907>
- [67] Food and Nutrition Board, National Academies (2019) *Dietary Reference Intakes (DRIs): Recommended Dietary Allowances and Adequate Intakes, Elements*. USA
- [68] Ralston KD, Birbilis N (2010) Effect of grain size on corrosion: a review. *Corrosion* 66:0750051–07500513. <https://doi.org/10.5006/1.3462912>
- [69] Atapour M, Pilchak AL, Frankel GS, Williams JC (2011) Corrosion behavior of  $\beta$  titanium alloys for biomedical applications. *Mater Sci Eng C* 31:885–891. <https://doi.org/10.1016/j.msec.2011.02.005>
- [70] Alfantazi AM, Moskalyk RR (2003) Processing of indium: a review. *Miner Eng* 16:687–694. [https://doi.org/10.1016/S0892-6875\(03\)00168-7](https://doi.org/10.1016/S0892-6875(03)00168-7)
- [71] Oliveira VMCA, Aguiar C, Vazquez AM et al (2014) Improving corrosion resistance of Ti–6Al–4V alloy through plasma-assisted PVD deposited nitride coatings. *Corros Sci* 88:317–327. <https://doi.org/10.1016/j.corsci.2014.07.047>
- [72] Yang J, Yang H, Yu H et al (2017) Corrosion behavior of additive manufactured Ti–6Al–4V alloy in NaCl solution. *Metall Mater Trans A Phys Metall Mater Sci* 48:3583–3593. <https://doi.org/10.1007/s11661-017-4087-9>
- [73] Czarnowska E, Wierzchoń T, Maranda-Niedbała A (1999) Properties of the surface layers on titanium alloy and their



biocompatibility in in vitro tests. *J Mater Process Technol* 92–93:190–194. [https://doi.org/10.1016/S0924-0136\(99\)00228-9](https://doi.org/10.1016/S0924-0136(99)00228-9)

- [74] Leon A, Levy GK, Ron T et al (2020) The effect of hot isostatic pressure on the corrosion performance of Ti–6Al–4V produced by an electron-beam melting additive manufacturing process. *Addit Manuf* 33:101039–101047. <https://doi.org/10.1016/j.addma.2020.101039>

**Publisher's Note** Springer Nature remains neutral with regard to jurisdictional claims in published maps and institutional affiliations.